Flexible Asymmetric Supercapacitor Assembled by Dahlia-Like Core-Shell Cobalt/Tin-Based Chalcogenide@Nickel Hydroxide Grown on Reduced Graphene Oxide

Huiru Sun,[‡a] Hanwen Zong,[‡a] Wenjun Huang, [a] Lejiao Duan, [a] Jingjing Dong, [b] Yuesheng Sun, [a] Zhongqi Lu, [a] Zhihan Yang, [a] Yawen Liu [a] and Jingquan Liu*[a]

a College of Materials Science and Engineering, Institute for Graphene Applied Technology Innovation, Collaborative Innovation Centre for Marine Biomass Fibers, Materials and Textiles of Shandong Province, Qingdao University, Qingdao 266071, P. R. China

b Key Laboratory of Colloid and Interface Chemistry, Ministry of Education, School of Chemistry and Chemical Engineering, Shandong University, Jinan 250100, P. R. China

‡ These authors contributed equally to this work.

***Corresponding Author**

jliu@qdu.edu.cn (Jingquan Liu)

Keywords: Cobalt/Tin-based chalcogenide; Dahlia-like structure; Core-shell structure; Reduced graphene oxide; Flexible asymmetric supercapacitors

2. Experimental

2.1. Preparation of hydrogel electrolyte

To prepare hydrogel electrolyte, 15 mL of DI water was slowly heated to 90 ^{o}C. Subsequently, 2 g of PVA was added and continued stirring for about 1 h until the dense and transparent homogeneous solution was obtained. Then, 10 mL of 1 M KOH transparent solution was slowly added when the above solution was cooled to 65 ^{o}C. Gel-like solution was acceptable until the prepared solution was utterly dissolved and cooled down. Generally, the PVA/KOH gel electrolyte is safer and more stable than the aqueous electrolytes.

2.2. Characterizations

The morphology and energy dispersive X-ray spectroscopy (EDS) and element mapping images of all samples with different microscopic sizes were characterized by a ZEISS Supra 55 scanning electron microscope (SEM) with accelerating voltage of 5 kV and 20 kV respectively. The elemental compositions of all samples were analyzed by X-ray photoelectron spectroscopy (XPS) employing a Thermo Scientific K-Alpha spectrometer (monochromatic Al Kα X-ray source, h = 1486.7 eV). All the prepared samples were characterized by X-ray diffraction (XRD) with a Rigaku DMax-Rb diffractometer under Cu Kα radiation (λ = 1.54056 Å). The porous properties of all the samples were obtained using N_2 adsorption/desorption studies utilizing ASAP2460, and their specific surface areas were calculated using the Brunaure-Emmett-Teller (BET) method. In addition, transmission electron microscope (TEM) images, high-resolution transmission electron microscopy (HRTEM) images, energy dispersive X-ray spectroscopy (EDS), element mapping images and selected area electron diffraction (SAED) of all the prepared products were characterized by a JEOL JEM 2100F transmission electron microscope at an acceleration voltage of 200 kV. Additionally, Raman spectroscopy using the Thermo Fischer DXR was employed to compare the D peak and G peak of the samples, which helped in analyzing their defect degree and graphitization degree.

2.3. Electrochemical measurements

All electrochemical data were collected using a Shanghai Chenhua electrochemical workstation (CHI 760E) at room temperature. 6 M KOH aqueous solution was used as the electrolyte throughout the experiment. To characterize the electrochemical performances, the rCSCTN was employed as the working electrode in the three-electrode tests. The platinum tablet and the mercuric oxide electrode were deployed as the counter electrode and reference electrode, respectively. Cyclic voltammetry (CV) and galvanostatic charge-discharge (GCD) tests were performed over a potential window ranging from 0 to 0.5 V. Additionally, electrical impedance spectroscopy (EIS) data were measured at a frequency range of 0.01 Hz to 10^5 Hz. To determine the specific capacitance C_s of the electrode, GCD curves were analyzed under various current densities, and the formula for calculating the specific capacitance C_s of the electrode is as follows:

$$C_s = \frac{I\Delta t}{m\Delta V} \quad \text{(S1)}$$

In this equation, the resulting C_s (F g^{-1}) is the specific capacitance of the working electrode. I (A) is the discharge current in the GCD curves, Δt (s) is the discharge time at diverse current densities, m (g) represents the mass of active material and ΔV (V) is the potential window of the working electrode.

2.4. Fabrication and electrochemical measurements of asymmetric supercapacitors (rCSCTN //AC)

To characterize the electrochemical performance of a solid asymmetric supercapacitor (ASC) device, we utilized rCSCTN as the cathode, with active carbon (AC) serving as the anode in two-electrode tests. We employed a KOH-based hydrogel electrolyte at ambient temperature, and collected electrochemical data. To achieve a high-performing ASC device, the amount of charge stored in each electrode must satisfy the equation ($q^+ = q^-$). We calculated the amount of charge stored using the following equation:

$$q = C \times m \times \Delta V \quad \text{(S2)}$$

Where C (F g^{-1}) means the specific capacitance of the electrode, m (g) means the weight of the active substance and ΔV (V) means the voltage window. The AC electrode was constructed by calculating the amount of electroactive component. The mass ratio of active carbon, acetylene black, and PVDF was designed at 8:1:1 to afford a mixture using ethanol as solvent. Acetylene black was used as conductive agent

and PVDF was utilized as binder. Subsequently, the mixture was transferred to a vacuum drying oven and dried at 50 ℃ for about 5 h. The obtained solid was then embedded in clean nickel foam, which was made into electrodes with a tablet press. Typically, the rCSCTN electrode and AC coated nickel foam electrode was adhered together with KOH-based hydrogel. Afterward, the prepared KOH-based hydrogel electrolyte was smeared evenly onto the surface of the rCSCTN electrode and AC electrode until it was largely saturated. Then the rCSCTN electrode and AC electrode coated nickel foam electrode were assembled with tiny pressure, allowing the formation of a thin separating layer of the KOH-based hydrogel electrolyte to achieve the rCSCTN//AC ASC device. Using the GCD curves, the specific capacitance (C_s) of the ASC could be figured out, the energy density E (W h kg^{-1}) and power density P (W kg^{-1}) could be figured out using the following two formulas:

$$E = \frac{1}{2} C_s \Delta V^2 \quad \text{(S3)}$$

$$P = E / \Delta t \quad \text{(S4)}$$

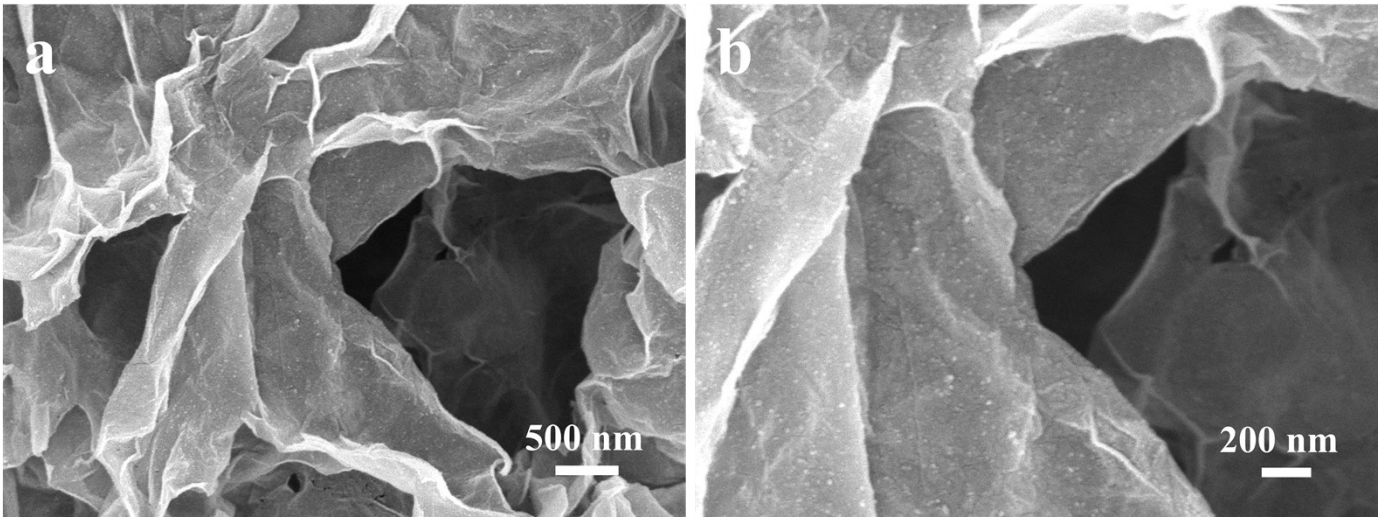

Fig. S1 SEM images of rGO

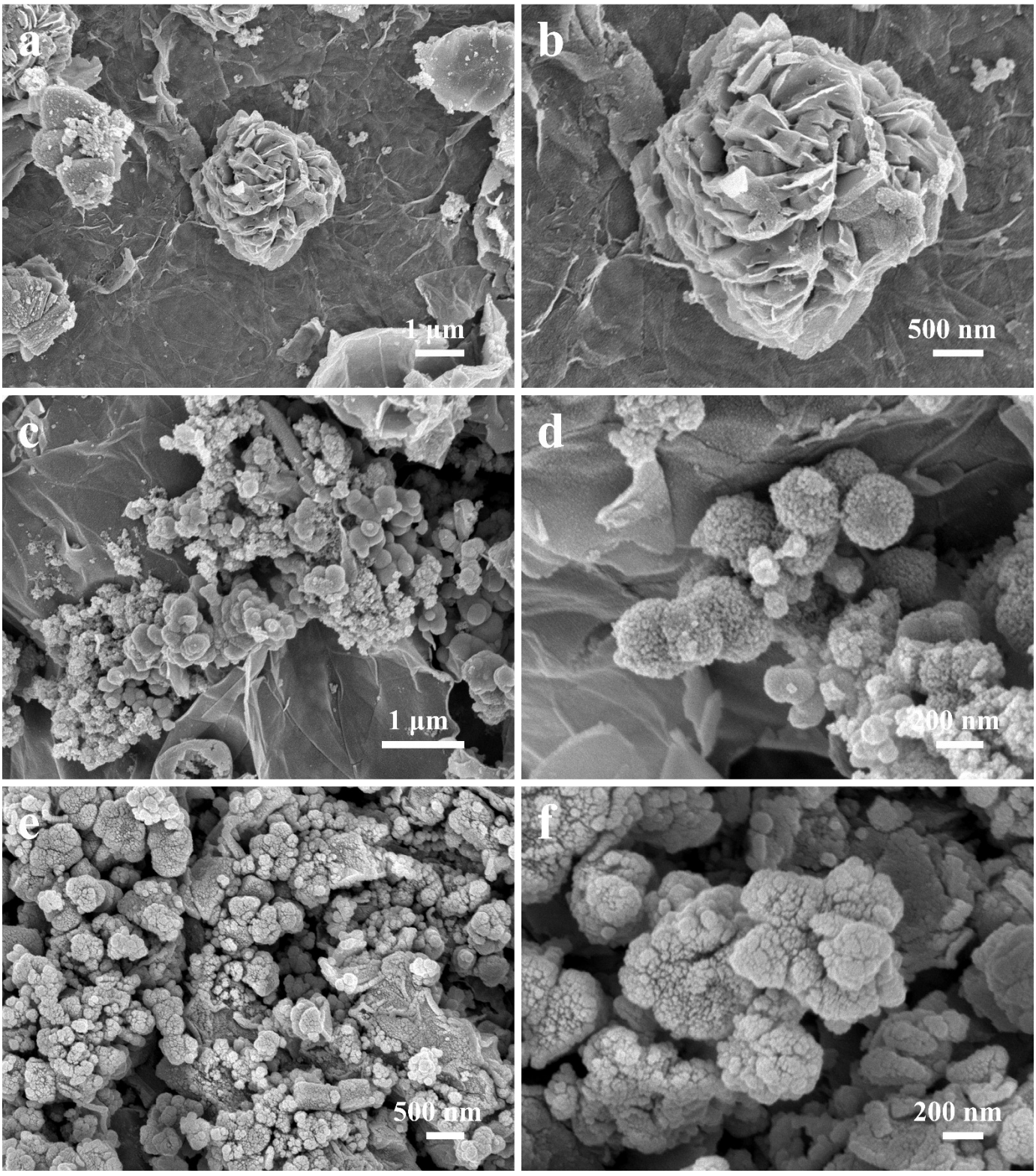

Fig. S2 SEM of rCSCTN-1(a-b), 2(c-d) and 3(e-f)

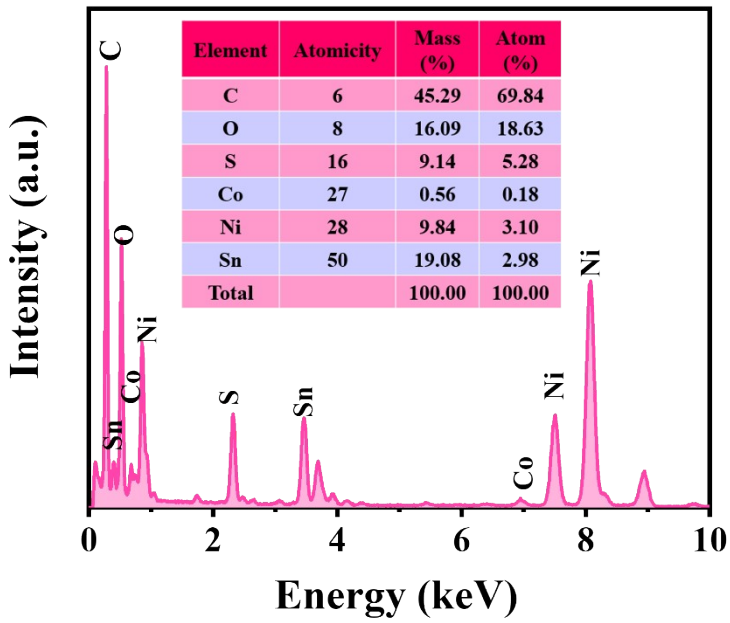

Element	Atomicity	Mass (%)	Atom (%)
C	6	45.29	69.84
O	8	16.09	18.63
S	16	9.14	5.28
Co	27	0.56	0.18
Ni	28	9.84	3.10
Sn	50	19.08	2.98
Total		100.00	100.00

Fig. S3 EDS spectrum of rCSCTN-4, the inset is a table of elemental analysis results.

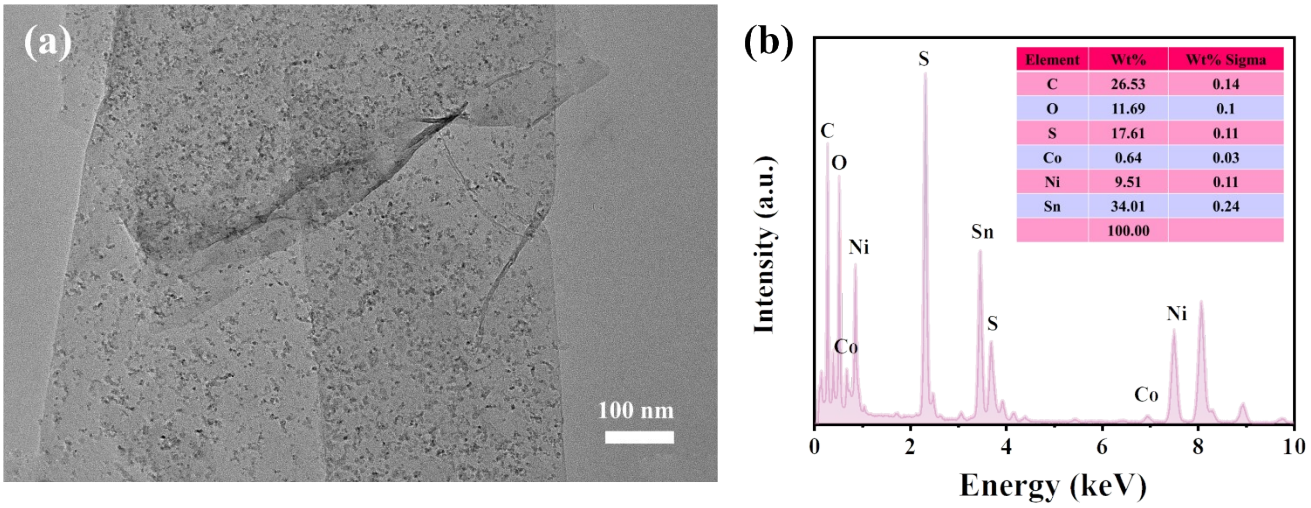

Element	Wt%	Wt% Sigma
C	26.53	0.14
O	11.69	0.1
S	17.61	0.11
Co	0.64	0.03
Ni	9.51	0.11
Sn	34.01	0.24
	100.00	

Fig. S4 (a) TEM images of rCSCTN-4. (b) EDS spectrum of rCSCTN-4.

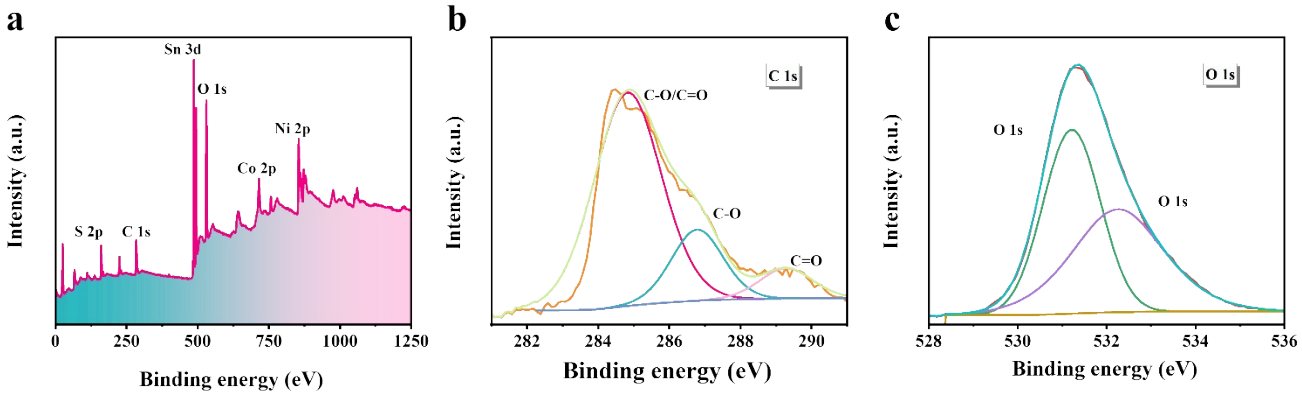

Fig. S5 (a) XPS survey spectrum of rCSCTN-4. In-depth XPS spectra of (b) C 1s and (c) O 1s on the rCSCTN-4.

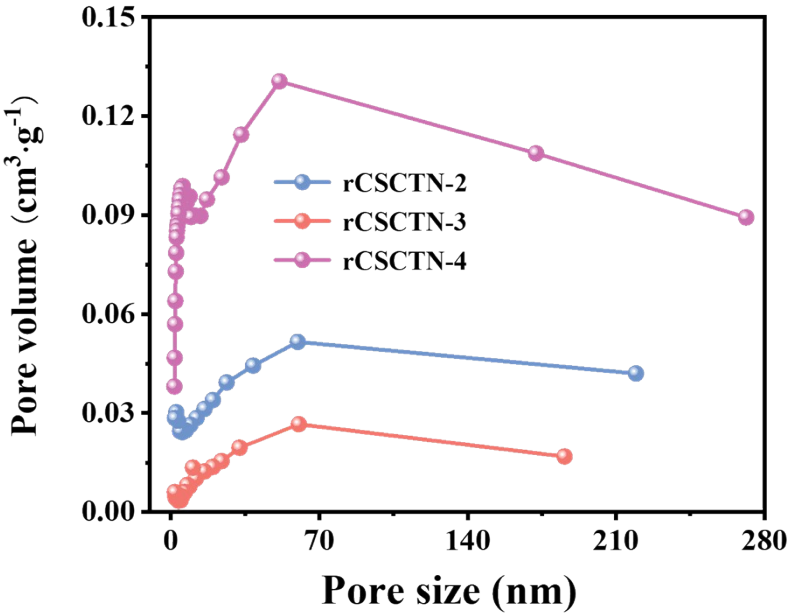

Fig. S6 Pore size distribution of rCSCTN-2, 3 and 4.

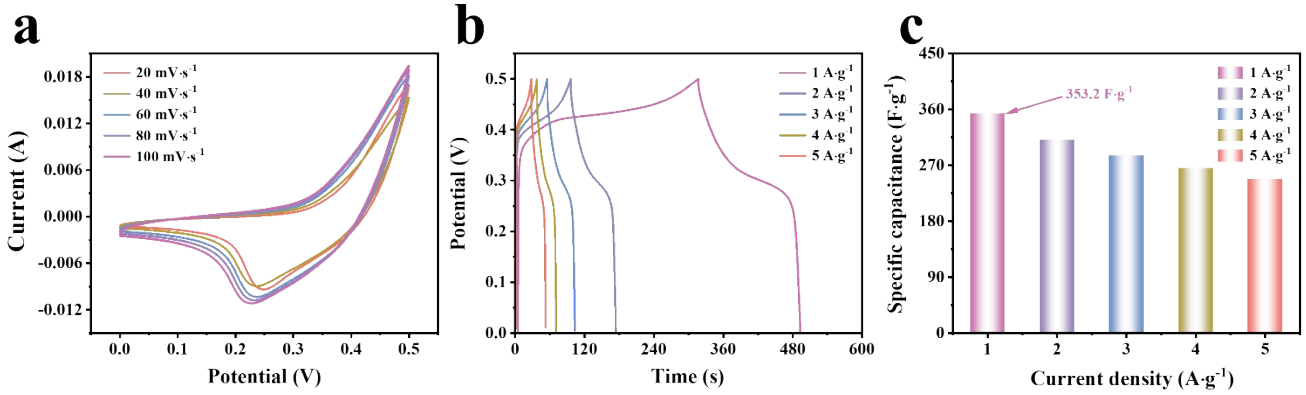

Fig. S7 (a) CV curves, (b) GCD curves of the prepared rCSCTN-3 electrode tested at different scan rates and current densities, respectively. (c) Comparison of the specific capacitance at the different current densities of the prepared rCSCTN-3 electrode.

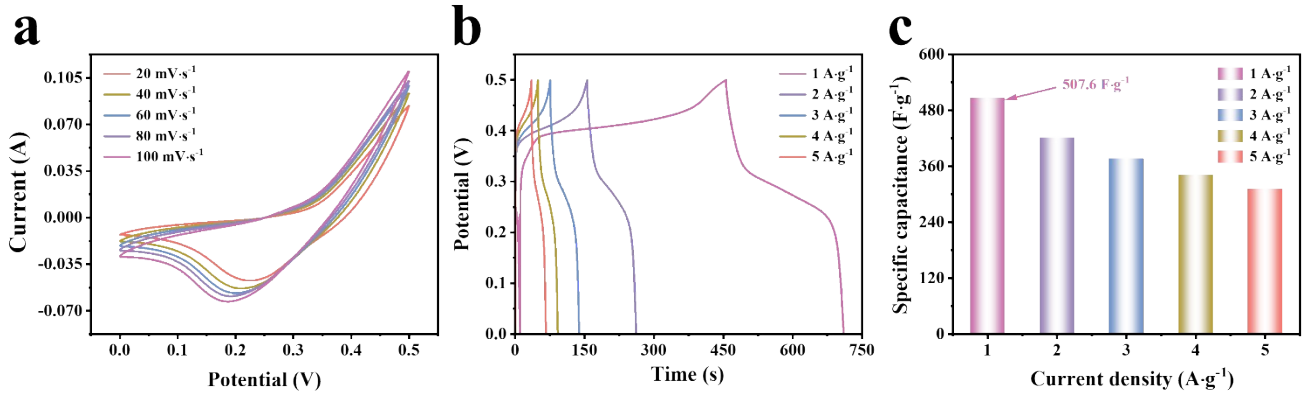

Fig. S8 (a) CV curves, (b) GCD curves of the prepared rCSCTN-2 electrode tested at different scan rates and current densities, respectively. (c) Comparison of the specific capacitance at the different current densities of the prepared rCSCTN-2 electrode.

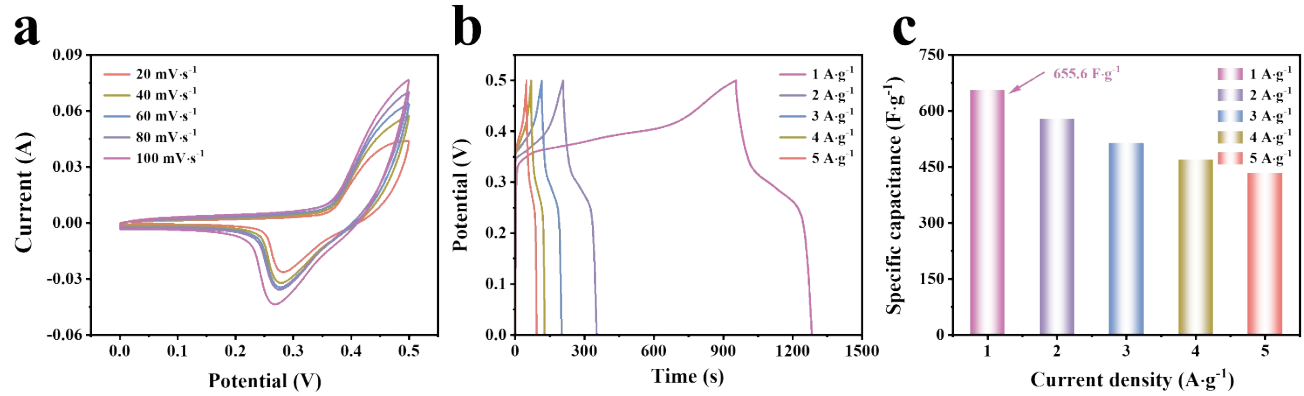

Fig. S9 (a) CV curves, (b) GCD curves of the prepared rCSCTN-1 electrode tested at different scan rates and current densities, respectively. (c) Comparison of the specific capacitance at the different current densities of the prepared rCSCTN-1 electrode.

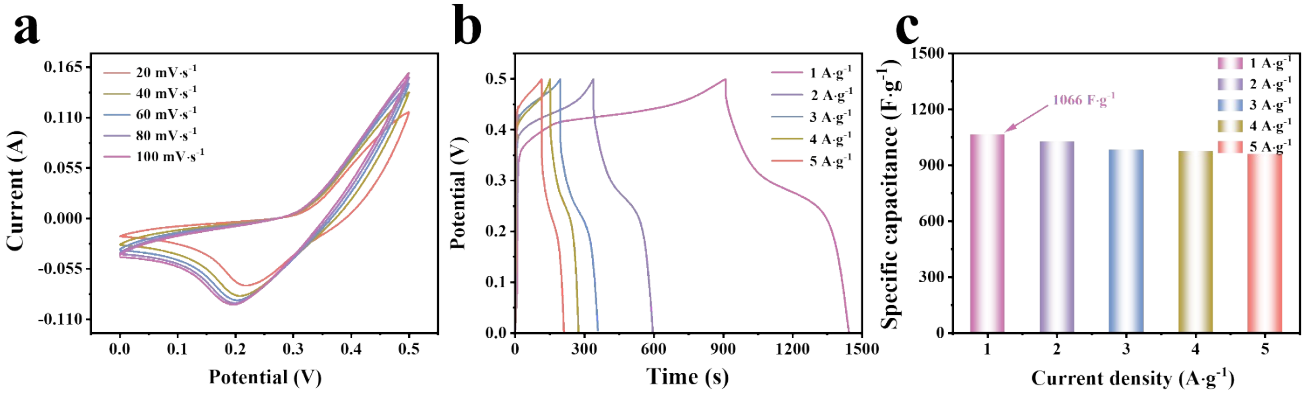

Fig. S10 (a) CV curves, (b) GCD curves of the prepared rCSCTN-4 electrode tested at different scan rates and current densities, respectively. (c) Comparison of the specific capacitance at the different current densities of the prepared rCSCTN-4 electrode.

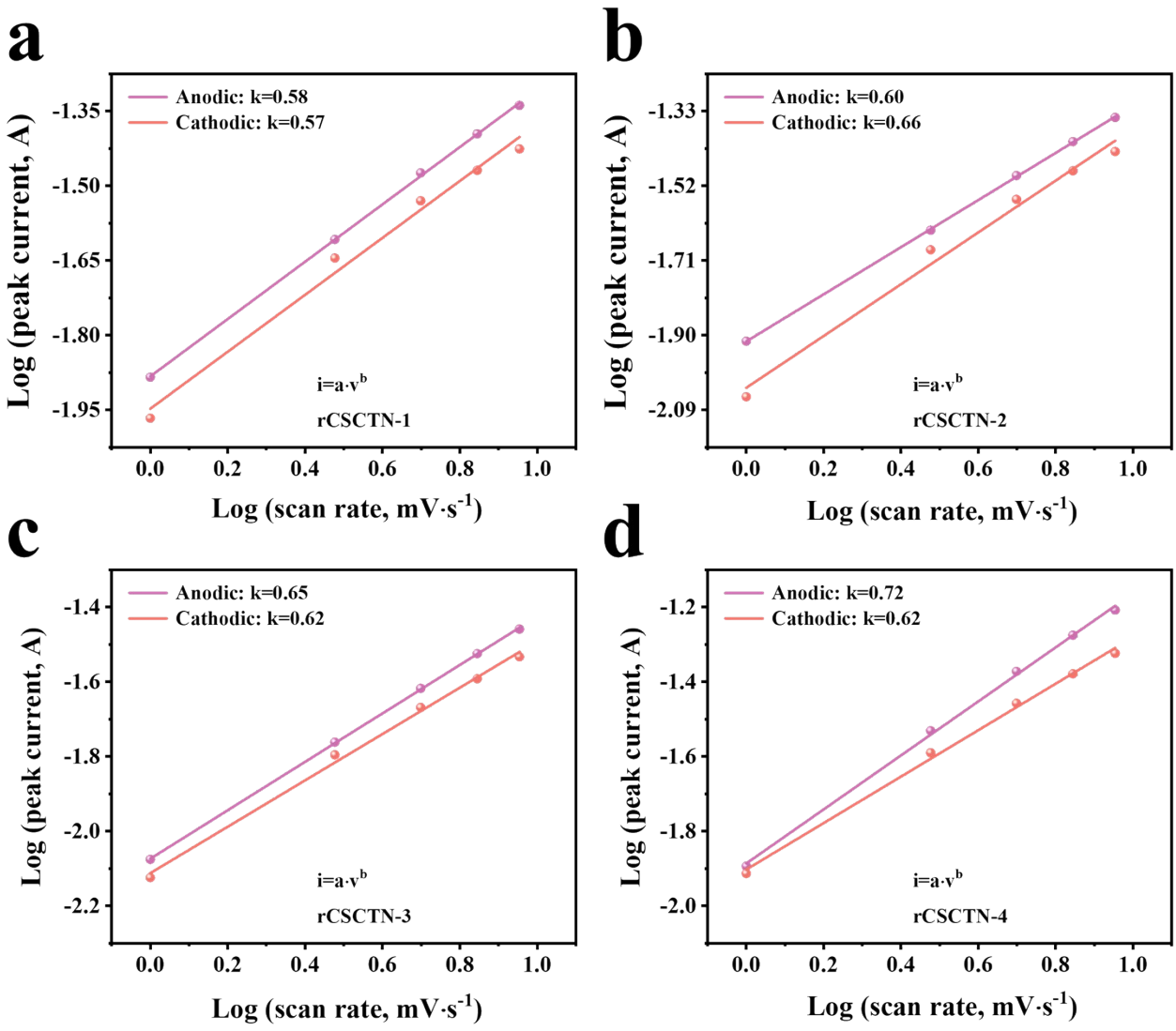

Fig. S11 Mechanistic pathway study on the rCSCTN electrodes. Plots of log *i* vs log *v* of the (a) rCSCTN-1, (b) rCSCTN-2, (c) rCSCTN-3, (d) rCSCTN-4 electrodes.

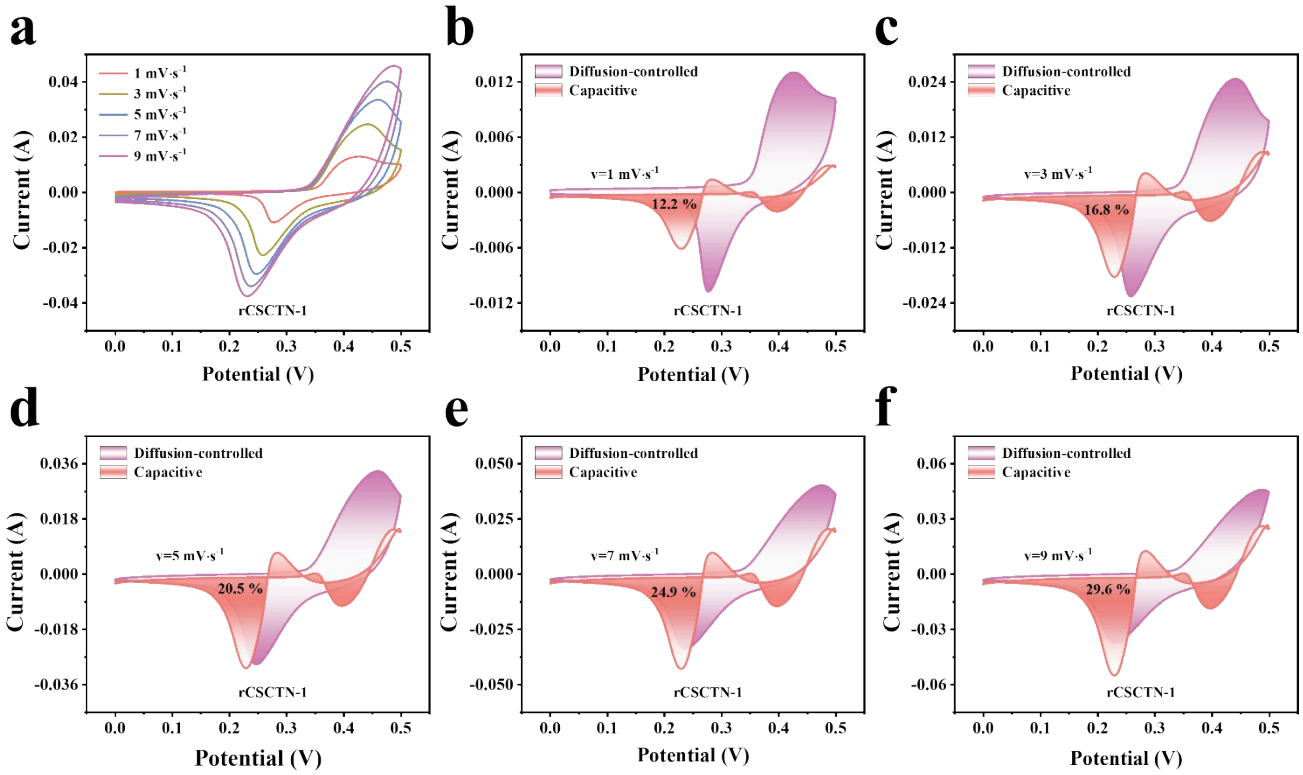

Fig. S12 Electrochemical behaviors and kinetic mechanism of the 1 electrode. (a) The CV curves of the rCSCTN-1 electrode at the different scan rates. (b-f) Separation of the diffusion and capacitive-controlled currents of the rCSCTN-1 electrode at a different scan rate of 1, 3, 5, 7 and 9 mV·s^{-1}

.

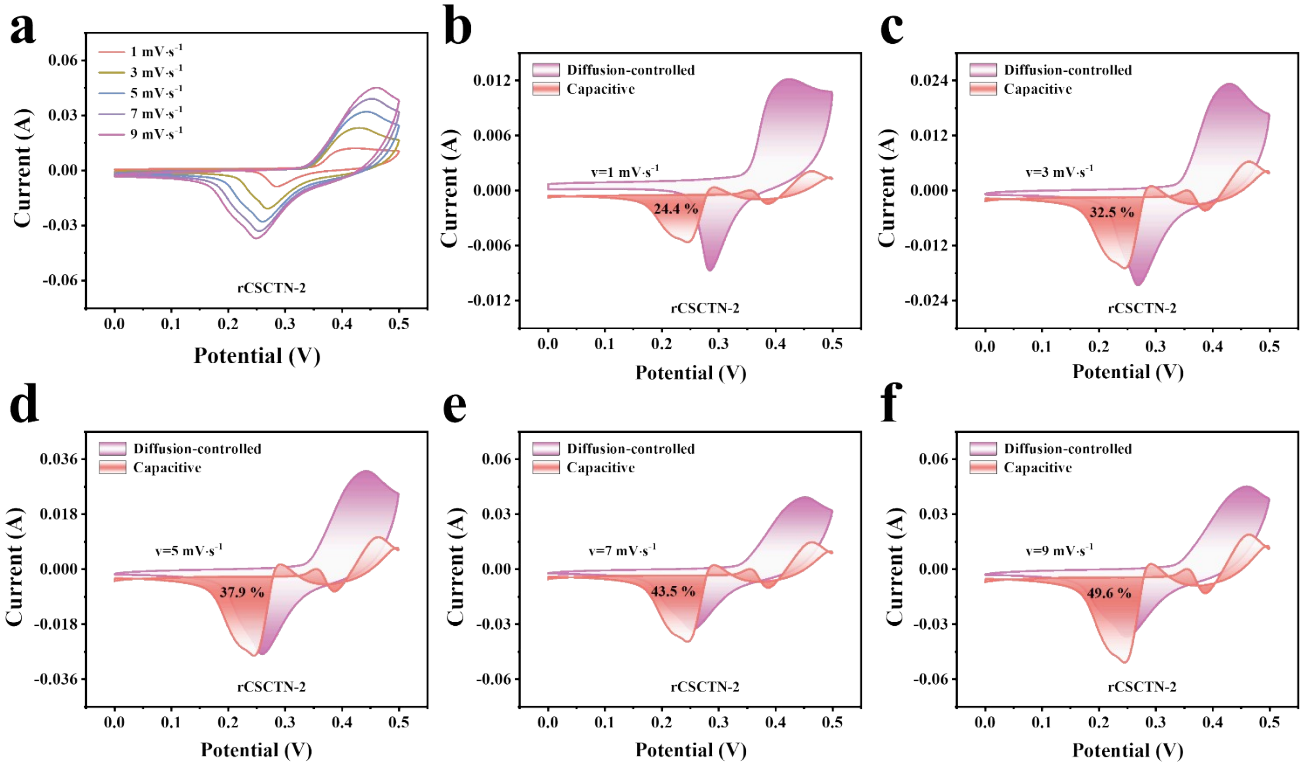

Fig. S13 Electrochemical behaviors and kinetic mechanism of the rCSCTN-2 electrode. (a) The CV curves of the rCSCTN-2 electrode at the different scan rates. (b-f) Separation of the diffusion and capacitive-controlled currents of the rCSCTN-2 electrode at a different scan rate of 1, 3, 5, 7 and 9 mV·s^{-1}

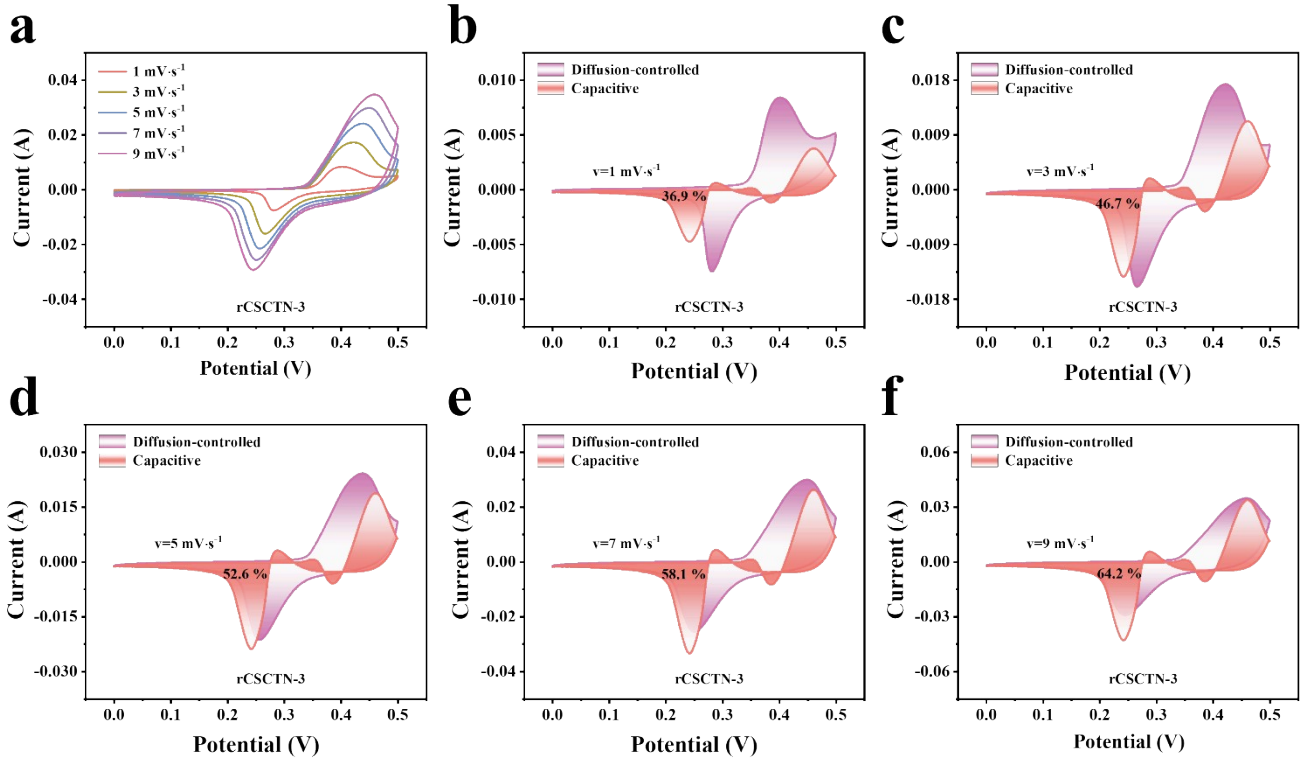

Fig. S14 Electrochemical behaviors and kinetic mechanism of the rCSCTN-3 electrode. (a) The CV curves of the rCSCTN-3 electrode at the different scan rates. (b-f) Separation of the diffusion and capacitive-controlled currents of the rCSCTN-3 electrode at a different scan rate of 1, 3, 5, 7 and 9 mV·s^{-1}

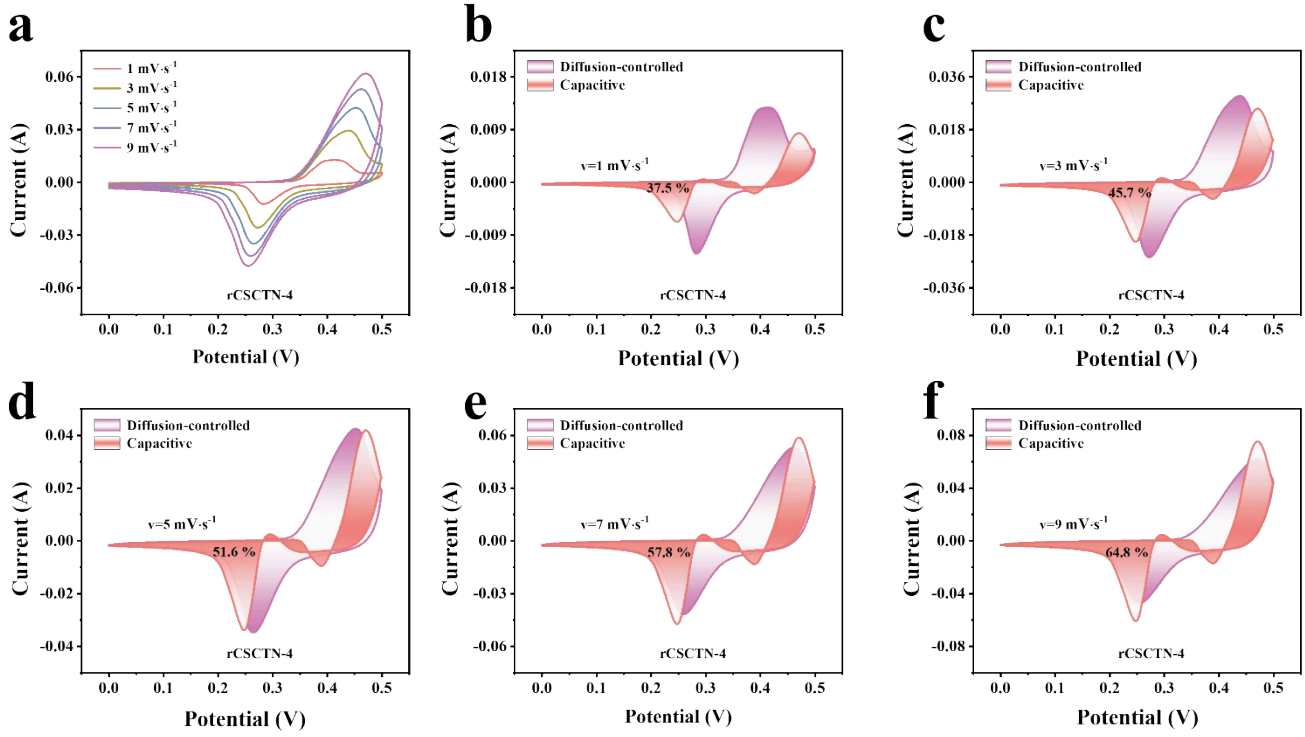

Fig. S15 Electrochemical behaviors and kinetic mechanism of the rCSCTN-4 electrode. (a) The CV curves of the rCSCTN-4 electrode at the different scan rates. (b-f) Separation of the diffusion and capacitive-controlled currents of the rCSCTN-4 electrode at a different scan rate of 1, 3, 5, 7 and 9 mV·s^{-1}

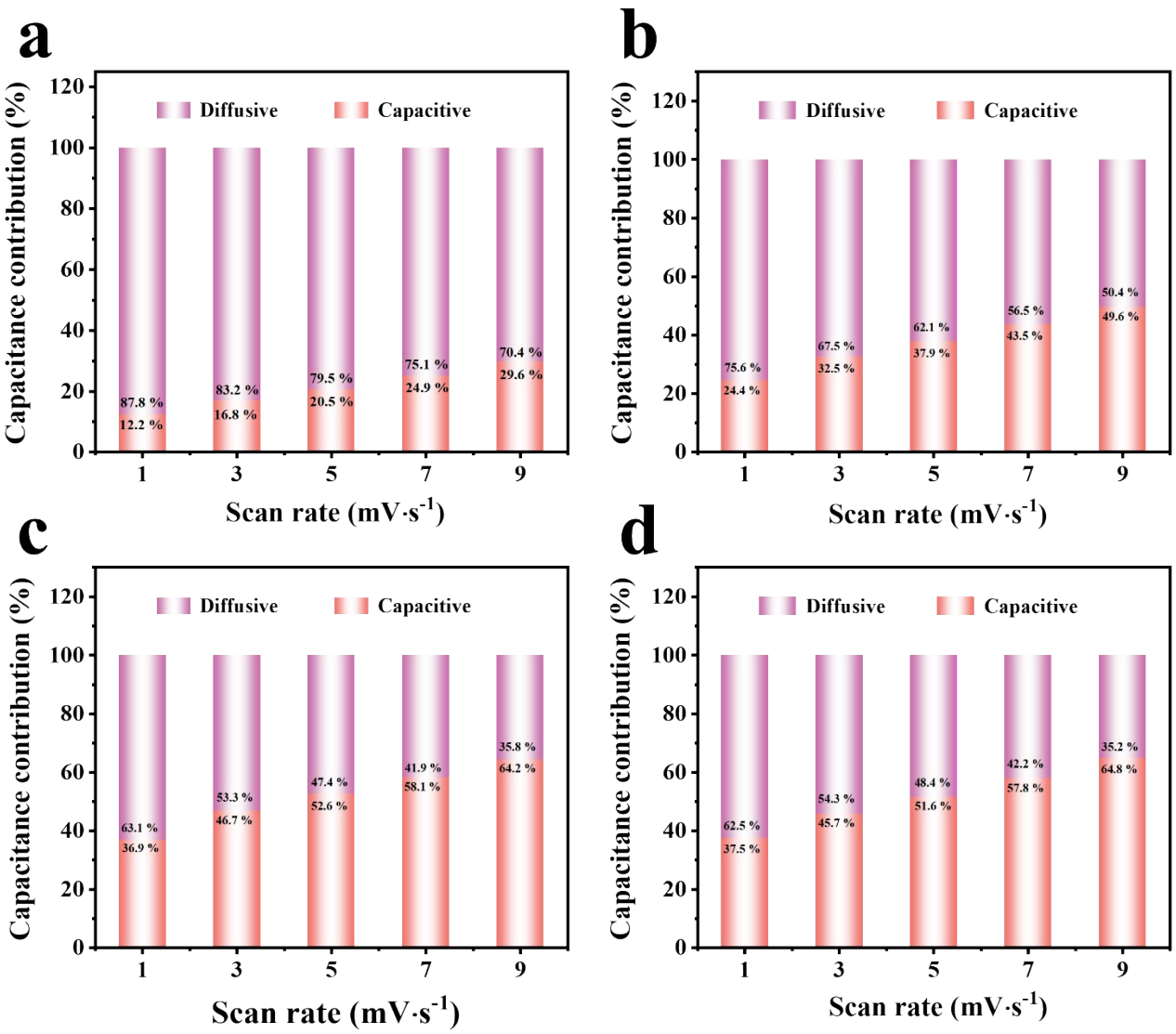

Fig. S16 Capacitance contribution rates of the (a) rCSCTN-1, (b) rCSCTN-2, (c) rCSCTN-3, (d) rCSCTN-4 electrodes at the diverse scan rates.

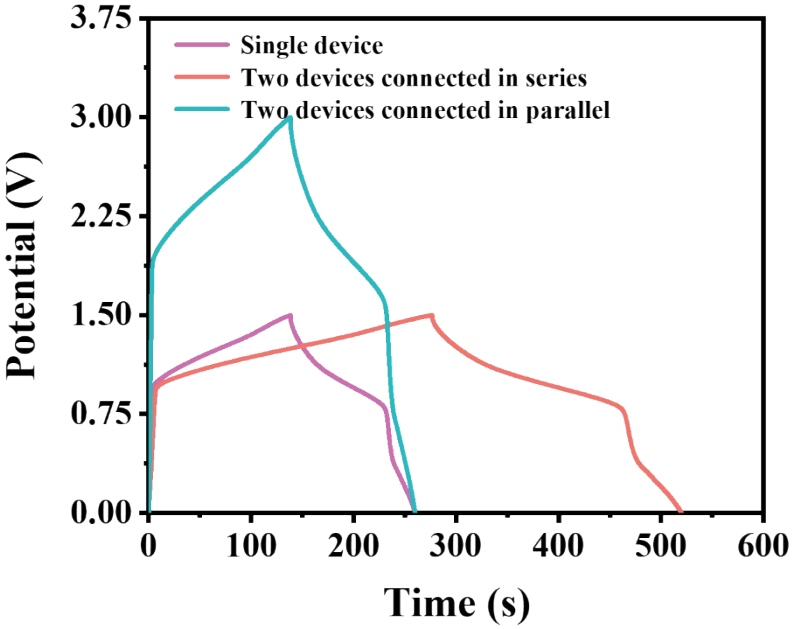

Fig. S17 GCD curves of a single device, two devices in parallels, and two ASS devices in series at the current density of 1A g^{-1}.

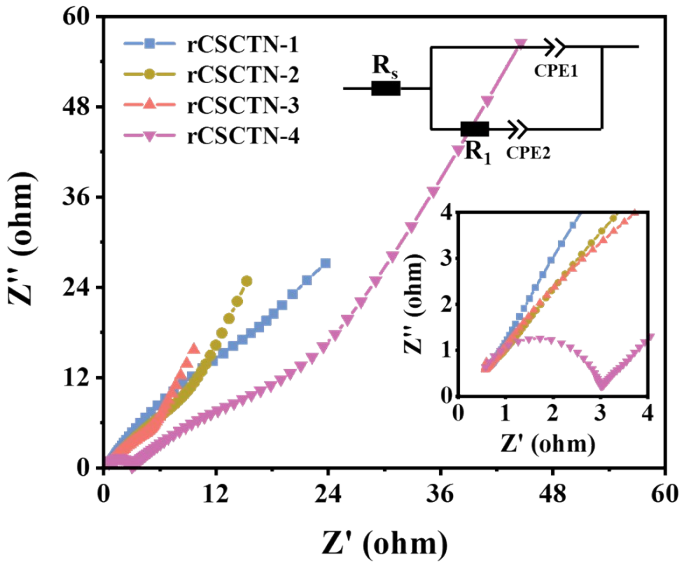

Fig. S18 Nyquist plots of rCSCTN-1, 2, 3 and 4 electrodes and fitting results of EIS.

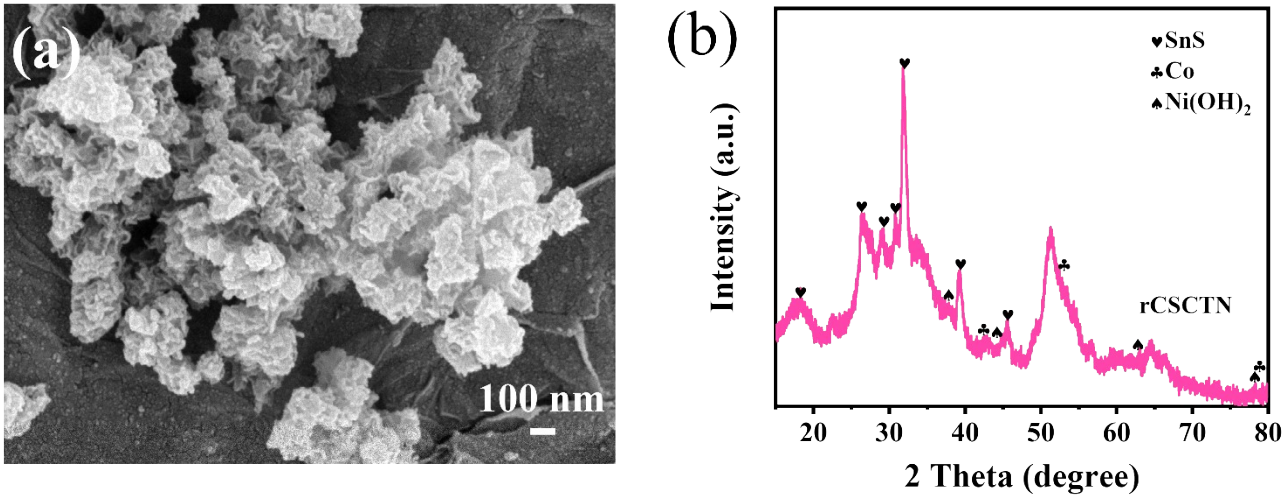

Fig. S19 SEM (a) and XRD (b) of rCSCTN after cycling.

Table S1 The specific surface area and pore volume of each sample.

Samples	**Specific surface area ($m^2 g^{-1}$)**	**Total pore volume ($cm^3 g^{-1}$)**
rCSCTN-2	10.302	0.043173
rCSCTN-3	5.405	0.276175
rCSCTN-4	40.785	0.096643

Table S2 The performance comparison between rCSCTN-4 and other supercapacitors References.

Electrodes	**Electrolyte**	**Current density**	**Specific capacitance**	**Ref.**
rCSCTN-4	6 M KOH	1.0 A g^{-1}	1066 F g^{-1}	This work
CSS/G/PEDOT/MnO_2	0.5 M Na_2SO_4	0.5 A g^{-1}	195.7 F g^{-1}	[1]
CCG/PANI-NFs	0.1 M HCl	0.3 A g^{-1}	210 F g^{-1}	[2]
L/rGO/C/MOFs	1 M $NaNO_3$	5 mV s^{-1}	390 F g^{-1}	[3]
SnO_2 –NW@CNFMs	6 M KOH	5 mV s^{-1}	420.1 F g^{-1}	[4]
PANI/TiO_2/GO	6 M KOH	1.0 A g^{-1}	430 F g^{-1}	[5]

HGPG	1 M H_2SO_4	1.0 A g^{-1}	437 F g^{-1}	[6]
GMs	6 M KOH	1.0 A g^{-1}	205 F g^{-1}	[7]
AC/Fe_3O_4	1 M Na_2SO_3	2.0 A g^{-1}	168.5 F g^{-1}	[8]

References

[1]. Tang, P . Y .; Han, L. J.; Zhang, L., Facile Synthesis of Graphite/PEDOT/MnO_2 Composites on Commercial Supercapacitor Separator Membranes as Flexible and High-Performance Supercapacitor Electrodes. Acs Appl Mater Inter 2014, 6 (13), 10506-10515.

[2]. Wu, Q.; Xu, Y . X.; Yao, Z. Y .; Liu, A. R.; Shi, G. Q., Supercapacitors Based on Flexible Graphene/Polyaniline Nanofiber Composite Films. Acs Nano 2010, 4 (4), 1963-1970.

[3]. Van Ngo, T.; Moussa, M.; Tung, T. T.; Coghlan, C.; Losic, D., Hybridization of MOFs and graphene: A new strategy for the synthesis of porous 3D carbon composites for high performing supercapacitors. Electrochimica Acta 2020, 329.

[4]. Chen, Y .; Wang, N.; Han, S.; Jensen, M.; Li, X. F.; Zhang, X. X., Synthesis of layered SnO_X nanostructure composite carbon hybrid nanofiber mats by blow-spinning for high performance pseodocapacitors. Electrochimica Acta 2021, 383.

[5]. Su, H. F.; Wang, T.; Zhang, S. Y .; Song, J. M.; Mao, C. J.; Niu, H. L.; Jin, B. K.; Wu, J. Y .; Tian, Y . P ., Facile synthesis of polyaniline/TiO_2/graphene oxide composite for high performance supercapacitors. Solid State Sciences 2012, 14 (6), 677-681.

[6]. Chen, N. N.; Ni, L.; Zhou, J. H.; Zhu, G. Y .; Kang, Q.; Zhang, Y .; Chen, S. Y .; Zhou, W. X.; Lu, C. L.; Chen, J.; Feng, X. M.; Wang, X. Z.; Guo, X. F.; Peng, L. M.; Ding, W. P .; Hou, W. H., Sandwich-Like Holey Graphene/PANI/Graphene Nanohybrid for Ultrahigh-Rate Supercapacitor. Acs Appl Energ Mater 2018, 1 (10), 5189-5197.

[7]. Wang, Y .; Shi, Z. Q.; Huang, Y .; Ma, Y . F.; Wang, C. Y .; Chen, M. M.; Chen, Y . S., Supercapacitor Devices Based on Graphene Materials. Journal of Physical Chemistry C 2009, 113 (30), 13103-13107.

[8]. Oh, I.; Kim, M.; Kim, J., Controlling hydrazine reduction to deposit iron oxides on oxidized activated carbon for supercapacitor application. Energy 2015, 86, 292-299.